Journal of Materials Chemistry A

Accepted Manuscript

ROYAL SOCIETY OF CHEMISTRY

www.rsc.org/materialsA

Journal of Materials Chemistry

ARTICLE

Received 00th July 2015,
Accepted 00th July 2015

DOI: 10.1039/x0xx00000x

www.rsc.org/

A core-level spectroscopic investigation of the preparation and electrochemical cycling of nitrogen-modified carbon as a model catalyst support

Steven T. Christensen[a], Dennis Nordlund[b], Timothy Olson[a], Katherine E. Hurst[a], Arrelaine A. Dameron[a], Kevin J. O'Neill[a], Justin B. Bult[a], Huyen Dinh[a], Thomas Gennett[a,†]

The synthesis and electrochemical cycling of platinum-ruthenium nanoparticles sputtered onto nitrogen-implanted highly-oriented-pyrolytic-graphite (HOPG) was studied with soft X-ray spectroscopy. The near edge X-ray absorption fine structure (NEXAFS) of the carbon 1*s*, nitrogen 1*s*, and oxygen 1*s* transitions were measured as a function of sample preparation and electrochemical cycling. The NEXAFS of the C 1*s* edge indicate defect formation in the graphitic (sp^2) network of the carbon support due to implantation. The primary nitrogen species include pyridinic, nitrilic, and graphitic with no evidence of pyrolic nitrogen. Upon exposure to ambient conditions, the carbon defects react and produce both –C=O and –C-OH species. Sputtering Pt:Ru and subsequent air exposure introduces more defects that react with ambient oxygen to increase the number of –C=O species. The samples also show signs of oxidization after implantation. Electrochemical cycling of the samples restores the C 1*s* fine structure associated with graphitic (sp^2) carbon and alters the concentration of nitrogen species associated with the nitrile functional groups. The cycling also induces platinum oxidation and ruthenium loss, determined from X-ray photoelectron spectroscopy (XPS) of the Pt 4*f*, Ru 3*d* and Ru 3*p*. The results provide useful evidence of the types of nitrogen species that are present after electrochemical processes which can be used in the rational design of future electrocatalyst systems.

1. Introduction

Carbon-based materials often serve as supports to disperse metallic nanoparticles for use as electrocatalysts. The carbon to catalyst metal interaction is relatively weak and most likely relies on van der Waals forces. This interaction does allow for charge transport that is critical for electro-catalysis but unfortunately does not prevent deleterious morphological changes during typical reaction conditions. For example, common electro-catalysts in polymer electrolyte membrane (PEM) fuel cells suffer degradation due to dissolution and/or coarsening of the nanostructured platinum group metals (PGMs). One approach to develop more stable nanostructured PGMs is to modify the carbon support chemistry and structure with the inclusion of hetero-atoms in the carbon matrix, e.g., nitrogen-modified carbon supports have demonstrated improved catalyst dispersion and stability. [1-13] The expectation is that the nitrogen species increases the support interaction with the metal to form a stronger bond versus the metal-carbon interaction. A strong interaction is expected to counteract the degradation resulting from the electrochemical environment. Density functional theory (DFT) predicts that certain, nitrogen species incorporated into carbon, such as pyridinic, should provide an interaction for metal species than the native carbon structures.[14-16] The mechanism can be more complex than direct localization of metal atoms on nitrogen moieties. DFT calculations by Holme *et al.*[14] indicated that Pt:Ru nanoparticles attach adjacent to nitrogen species which was also supported by some experimental evidence[16]. The effect of nitrogen modification has lead to reduced dissolution of Pt:Ru nanoparticles[10] and longer durability for complete fuel cell systems[11].

What may be underemphasized in efforts to enhance catalyst-support interactions is the response of a modified support to the same catalytic environment that the catalyst experiences. The expectation is that the nitrogen species will be stable with respect to the electrochemical environment. The inclusion of nitrogen introduces changes to the electronic and physical structure of the carbon support. It is possible that degradation pathways of the catalyst support could result. In

[a] National Renewable Energy Laboratory, 15013 Denver West Pkwy, Golden, Colorado, 80401, USA
[b] Stanford Synchrotron Radiation Lightsource, SLAC National Accelerator Laboratory, 2575 Sand Hill Rd, Menlo Park, California, 94023, USA.
† Corresponding author.

parallel, the different nitrogen moieties may react differently to the electrochemistry. Understanding how the nitrogen reacts to the electrochemical environment will benefit efforts to design a more robust catalyst-support system, especially if specific nitrogen species are found to persist following electrochemical processes.

Nitrogen incorporation into carbon has been studied extensively and we refer specifically to Zhou *et al.* how have reviewed the topic in the context of catalyst supports.[17] Core-level spectroscopy such as X-ray photoelectron spectroscopy (XPS) has been often employed to characterize the system(s) given the sensitivity of the chemical environment in the final state. An electron binding energy shift, often referred to as the chemical shift, is an indirect probe to identify chemical structures. Through XPS investigations, the predominant nitrogen species identified to improve the catalysts are derivatives of pyridine, pyrrole, graphitic, and quaternary that are integrated into the graphitic carbon structures.[9, 15, 18, 19] X-ray absorption spectroscopy (XAS) is another core-level spectroscopy technique that can provide rich information regarding chemical structure through the local mapping of the partial, unoccupied density of states (DOS).[20] Specifically, for the light elements (e.g. C, N and O) the anti-bonding states of *p*-character are directly probed in the NEXAFS within the dipole selection rule. This sensitivity and richness of NEXAFS to functional groups with different chemical bonds typically allows for a definitive identification of nitrogen species in modified carbon supports.

As indicated above, the effects of catalytic processes on the nitrogen-modified supports are needed to establish the viability of an enhanced support interaction and to identify the most promising strategies to successful implementation. We investigate the evolution of the carbon, nitrogen, oxygen and metal species as a function of the nitrogen-incorporation process, metal deposition (platinum-ruthenium), and electrochemical cycling of the support. The electrochemical cycling consisted of sweeping the voltage of an electrochemical half-cell in acidic conditions. This is intended as a model catalytic environment that could induce changes to both the modified substrate and deposited metal. The NEXAFS of the C, N, and O K edges and XPS of the Pt:Ru provided a measure of the evolution of the local atomic environment.

Our work focuses specifically on a model catalyst system for direct methanol fuel cells (DMFCs) where Pt:Ru alloy is deposited on nitrogen-modified highly oriented pyrolytic graphite (HOPG) substrates. While the emphasis of this paper deals with the evolution of the HOPG support, the impact of enhanced support interactions is particularly important, as dissolution of ruthenium is a critical issue for DMFC catalysts. HOPG was selected as it provides a convenient substrate for characterization of the nitrogen incorporation, metal deposition and post-mortem electrochemical cycling. In this study, the nitrogen modification was accomplished by ion implantation, while the Pt:Ru was deposited via magnetron sputtering, which we and others have reported previously.[9, 10, 19] Ion implantation has been shown to produce several different nitrogen species in graphitic carbons such as pyridinic, nitrilic, pyrrolic, cyano and graphitic.[9, 21, 22] The metal deposition process via sputtering was previously reported to deposit small, uniform Pt:Ru nanoparticles.[23]

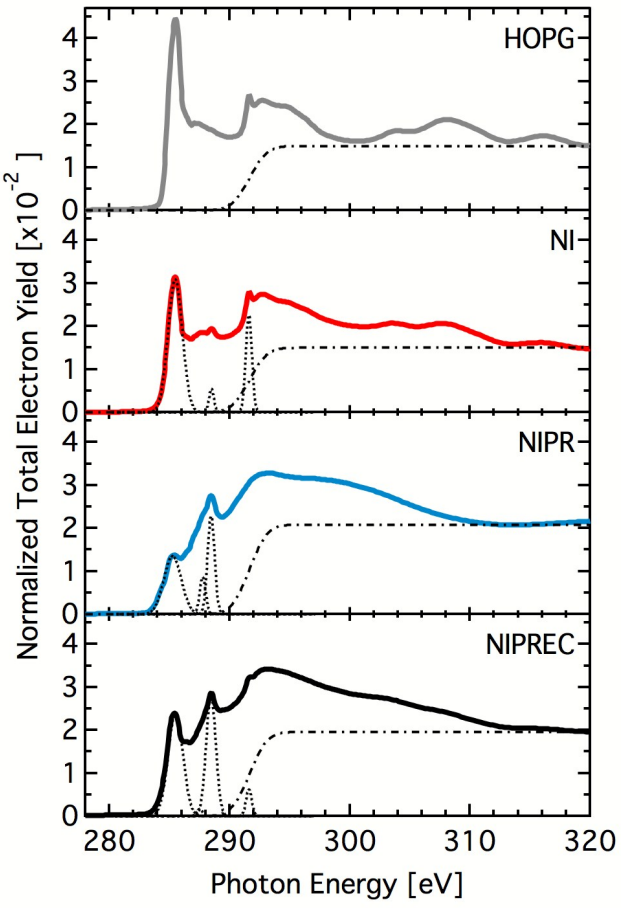

Figure 1. Carbon 1*s* NEXAFS data for the sample preparation conditions: cleaved HOPG, nitrogen implanted (NI), nitrogen-implanted-platinum-ruthenium deposited (NIPR), and NIPR electrochemically cycled (NIPREC). Also plotted are the results from the fitting analysis. The changes of π* at ~285 eV and other features show an evolution of the carbon specie from a highly ordered to heterogeneous structure.

2. Results and Discussion

2.1 C 1*s* NEXAFS

The normalized C 1*s* → π* NEXAFS are plotted in Figure 1 for: an unmodified HOPG reference scan; a nitrogen implanted (NI) HOPG; a nitrogen implanted and Pt:Ru sputtered (NIPR) HOPG;, and electrochemically cycled (NIPREC) nitrogen implanted and Pt:Ru sputtered HOPG. Figure 1 also includes peaks extracted from fitting analysis. Table 1 provides the peak positions for fitting analysis of the C 1s spectra in the 1*s* → 1π* region. The 1*s* → 1π* region is useful for identifying carbon species by comparison of molecular and condensed phases in the NEXAFS literature. The main C 1s → 1 σ * contributions are found around 292-294 eV (with the core excition at around 291.65 eV[24]) and multiple scattering effects sensitive to structural order can be found at higher energies in the pure HOPG. The spectra in Figure 1 (and subsequent NEXAFS

figures) are taken on different samples for the specific sample conditions.

The HOPG sample shows a well-defined π-resonance (at 285.5 eV) and sharp resonance at 291.7 eV. The peak near 285.5 eV corresponds to the aromatic π* of the graphitic planes (–C=C–) and is an indication of the degree of unperturbed sp^2 sites in the carbon lattice. The sharp C 1s core exciton at 291.65 eV, present in all conditions, marks the transition to the σ* region. This core-exciton is very sensitive to structural order.[24] The behavior of these two features when considered as a function of sample preparation provides general information on how the number of carbon in sp^2 configuration and the long-range order of the carbon atoms is affected. In all sample preparations the π* and exciton peak are reduced, which indicates a disruption of the sp^2 bonding and long-range order. This is likely due to point defects due to bombardment during ion implantation and sputtering. In order to compare preparation conditions, we define the ratio π* / σ* as the ratio between the π* peak height and the maximum of the σ* region. The NIPREC shows an increased π* / σ* ratio, suggesting that electrochemical cycling has the effect to restore long-range order in the sp^2 plane.

All of the sample preparation conditions show features between 285 and 292 eV that are due to functionalization of the sp^2 carbon lattice. We note that these features are rather broad and there are several components that are difficult to extract reliably, which it not surprising given the heterogeneity expected from implantation, sputtering, and/or subsequent exposure to air. We applied peak fitting analysis to aid in identifying the possible carbon species responsible for the NEXAFS. The region 286-290 eV can be associated with many functional groups; we limit the discussion to major H, C, O and N combinations. Carboxylic species, -C=O, have been identified at 288.5 eV.[20, 25-27] The most dominant peak occurs near 288.5 eV for all preparation conditions, which we assign from literature to 1s → π* for -C=O carboxylic species. The region of 286-287 eV in the C 1*s* NEXAFS contains several different carbon species, carbon-oxygen and carbon-nitrogen including: aromatic –C-OH;[28] and sp^2 –C-OH;[29] pyrrolic –C-N-C-;[30, 31] and nitrilic –C≡N (286.2 eV).[32] The fitting analysis yielded a peak near 286.1 eV. We assign this feature to a "dangling" nitrilic –C≡N, which will be further discussed in more detail for the N 1*s* NEXAFS (Fig 2). The features near 288 eV for NI and NIPR are assigned to –C≡N species in pyridinic structure based on previous work on carbon nitride films.[33] We also note the –C-H bond is found at 287.5 eV.[20] Molecular pyridinic –C-N-C- has been identified at 287.4 eV[34].

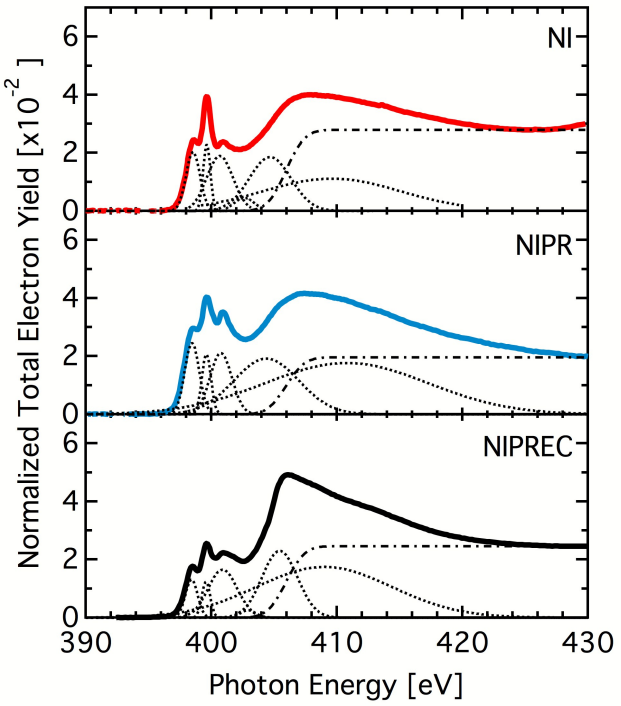

Figure 2. NEXAFS data and fits for Nitrogen 1*s* absorption edge for NI, NIPR, and NIPREC sample preparation conditions. Nitrogen implantation produces pyridinic, nitrilic, and graphitic species as observed by the peaks near 399 eV. Subsequent processing causes these specific functionalities to be reduced but the overall nitrogen content does not change significantly. See Table 2.

As mentioned above the electrochemical cycling leads to features that are associated with long-range order in carbon. We propose that the electrochemistry has the ability to do work on the system to remove and/or reform carbon defects formed by the substrate preparation. The result produces NEXAFS that indicates a carbon structure with long-range order improved to that of the as processed. The impact to the electrochemistry is that carbon defects do not persist in that environment and therefore their participation in electrochemical processes would come at a diminishing level.

2.2 N 1s NEXAFS

Figure 2 shows the normalized N 1*s* NEXAFS data and fitting results. Based on previous work under similar conditions the estimated ion implantation depth into the HOPG is 5-10 nm.[9] The reported spectra are from the total electron yield, which was selected based on best signal to background. Auger electron yield was also collected but did not exhibit suitable signal-to-background for analysis. The peak positions from the fitting analysis are given in Table 2. Samples implanted with nitrogen (NI, NIPR, NIPREC) all have common features in the 1*s* → 1π* region (E_γ < 406.0 eV) in the form of three peaks situated near 398.4, 399.5, and 400.7 eV. Table 2 also provides the total area of the respective NEXAFS spectra prior to intensity normalization. This total area provides a measure of the absolute nitrogen content resulting from the sample preparation. The data in Figure 2 have been plotted after being normalized to the respective areas in Table 2. The nitrogen content increases from NI to NIPR, which is consistent with previous XPS studies[35] Most important, there is no significant loss of nitrogen content from electrochemical cycling.

Nitrogen functionalization and associated NEXAFS features have been well documented in the literature for nitrogen modified carbon materials, i.e. the N 1s → π* transitions for pyridinic (398.3 eV), nitrilic (399.5 eV), and graphitic (400.7 eV) nitrogen species.[21, 22, 32, 36-39] Shimoyama *et al.* studied nitrogen implanted HOPG and reported the incident X-ray angle dependence of these features, demonstrating a structure where the nitrilic nitrogen was connected to the edge sites of

graphitic sheets and that the graphitic nitrogen π orbitals were coplanar with the graphitic carbon π orbitals.[21, 22] Graphitic, pyridinic and nitrilic nitrogen and their angular dependence in XAS have also been reported for sub-percent concentration of nitrogen in graphene.[39] We did not observe any angle dependence of the intensity in these peaks, which demonstrate the absence of well-defined high-symmetry sites of the nitrogen-containing functional groups . We note that –N=O has been reported at 399.1 eV.[20] Also, the N 1s NEXAFS of porphyrin gives N 1s → π* resonances near 398.3 eV and 400.3 eV.[40, 41] Pyrrole has been assigned to the C 1s → 1π* peak at 288.3 eV.[31], and to the N1s → π* transition at 402.1-3 eV.[30, 31] Since spectral features not clearly distinguished in any of our N1s NEXAFS data, we assume a limited presence of pyrrolic nitrogen in our samples.

The N 1s → σ* region (E_γ > 406.0 eV) is more straightforward to interpret than the C 1s → σ* region since the signal is solely associated with the nitrogen containing functional groups and not the carbon matrix. Graphitic nitrogen can be associated with a σ* resonance at 405 eV [32], pyridinic C-N σ* features in pyridine have been observed at 408 eV and 414 eV.[34] In our case, for the NI and NIPR the σ* region is rather broad and featureless which indicate a multitude of local structures with varying C-N bond lengths.

Electrochemical cycling produces dramatic changes in both the π* and σ* N 1s NEXAFS. The π* / σ* ratios are roughly equivalent for the NI and NIPR cases where as the π* are approximately half the height of the σ* region for NIPREC. The σ* transitions for NI and NIPR show broad continuum resonances consistent with structural heterogeneity. The σ* region for the NIPREC condition exhibit a well-defined peak at around 406 eV as well as increased fine structure at higher energy. The changes in the N 1s due to electrochemical cycling are consistent with the C 1s NEXAFS that show reduced functionalization and increased carbon lattice order. Specifically, the formation of a well defined σ* is consistent with a more narrow distribution of species with similar bond length.[20]

The reduction of primarily the nitrilic peak at 399.5 eV is indicative of the loss of nitrile groups. This is not surprising as the –C≡N would either be attached the basal plane of the HOPG or at sp^3 carbon defects. The total area, however, from Table 2 would suggest that nitrogen is not lost during electrochemical cycling. Again we note the data shown in Figure 2 has been normalized by the respective area values in Figure 2. The reduced π*/σ* ratio is indicative of a reduction of unsaturated nitrogen local configuration (strong π* resonances) and an increase of saturated nitrogen local configurations that are not graphitic. We propose that the nitrogen in the nitrile groups and other polydisperse species that originate in sample preparation could be converted to a form where π bonding is minimal. Some π bonding is in any case retained after electrochemical cycling as evident in Figure 2.

Several amine groups, such as those in tetrakisdimethylamino silane, are candidates that demonstrate similar spectral features in the NEXAFS.[42, 43] The actual nature

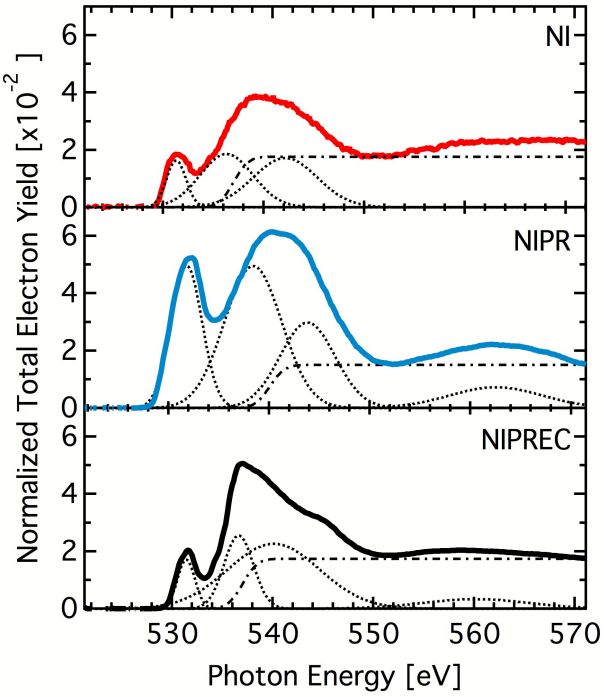

Figure 3. Oxygen 1*s* NEXAFS data and fits for the sample preparation conditions. Oxygen species due to air exposure become less polydisperse due to electrochemical cycling (NIPREC). This correlates with losses of polydisperse carbon from the C 1s NEXAFS.

of the nitrogen groups would be a protonated $–NH3^+$ (ammonium) due to the acidic conditions of the electrochemical cycling. After cycling the ammonium may return to amino, $-NH_2$, otherwise an ammonium salt would need to form. This was not observed nor expected. The spectral differences for NEXAFS would not be distinguishable for amino or ammonium with our experimental capabilities in any case. For convenience, we will treat amine and ammonium as the same and refer to them as *amino*.

The observed restructuring of nitrogen groups upon electrochemical cycling gives insight into the moieties that are likely to persist throughout the catalyst life span. From the changes described, there remains pryridinic, some nitrilic, graphitc and possible amino groups. From the DFT studies, we understand that the pyridinic groups would be best for interacting with the metal catalyst and by this same measure the graphitic are not likely to be important for metal interactions. The inclusion of nitrilic and possibly amino groups has not been considered within the literature. These moieties could impact both the interaction with the metal atoms and electrochemical processes. The pyridinic, nitrilic, and amino groups all act as Lewis bases and lie within close proximity to catalyst sites.

2.3 O 1s NEXAFS

In Figure 3 we show the data and fitting results for the O 1*s* NEXAFS for the various sample conditions. The fitted peak positions and the total area prior to normalization for the O 1s spectra are given in Table 3. A broad peak in the O 1s → π* region (E_γ < 537.0 eV) located near 532 eV is present in all the

samples. This peak is typically associated with –C=O species although it is somewhat insensitive to the type of carbonyl species (e.g. carboxylic vs. ketone). The peak could also be related to –N=O species. A reduction in intensity of the peak at 532 eV is directly related to a loss of –R=O species where 'R' could be carbon or nitrogen. The π* for the NIPR is nearly equal to the 1s →σ* (E_γ > 537.0 eV) whereas it is much less for the NI and NIPREC. We interpret this as the extended oxidation due to exposure to air after the Pt:Ru deposition. The loss of the π* peak for NIPREC is suggestive of a loss of –C=O and possible –N=O. The O 1s →σ* region displays peaks near 536 and 539 eV, which can be associated with single bonded oxygen, e.g. –C-O-C– and –OH. Peaks can also be found near 544 and 560 eV. (Note: that the σ* resonances for carbonyl (-C=O) have been reported at 544.0 eV.[20])

Several changes occur in the O 1s NEXAFS in each processing step. We find that the total area of the O 1s NEXAFS increases going from NI to NIPR to NIPREC (Table 3). This shows that each step introduces more oxygen species with NIPR causing the greatest increase. With respect to the spectra in Figure 3, the height of the 1s → π* is nearly equivalent to the 1s →σ* for the NIPR where as the NI and NIPREC have a π* that are approximately one third the σ*. The NI treatment introduces some oxygen species at the expense of sp^2 carbon based on the reduction of the π* peak in the C 1s spectra. The subdued π* peak in the NI condition and the σ* near 536 eV could originate for –OH upon exposure to ambient moisture. The NIPR condition introduces more

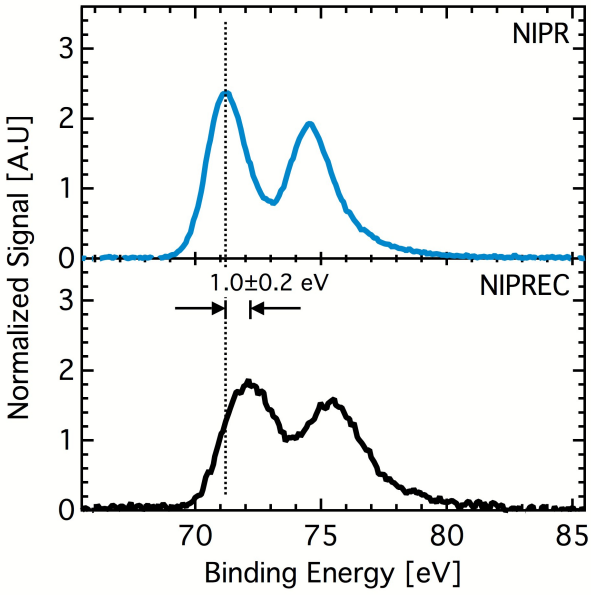

Figure 4. Platinum 4*f* XPS data for the NIPR and NIPREC sample preparation conditions. The NIPREC binding energy data has shifted +1 eV higher and is broadened. The dashed line marks the Pt $4f_{7/2}$ binding energy of 71.2 eV.

oxygen species in the sp^2 carbon. These species tend to have a greater degree of –C=O. Similar to the nitrogen XAS, we observe the greatest changes to the spectra after electrochemical cycling. The π* peak is greatly reduced in the NIPREC compared to the NIPR, which clearly indicates a decrease of the –C=O species. The peaks in the 1s →σ* also become more well defined, indicating a loss of polydisperse oxygen species, similar to the nitrogen functionalized groups. Similar to the argument for the formation of amino groups based on the N 1s, the O 1s spectra exhibit 1s →σ* similar to several alcohols investigated by Hitchcock et al.[42] Thus we hypothesize that the electrochemical cycling increases the amount of –OH groups via protonation in an acidic media.

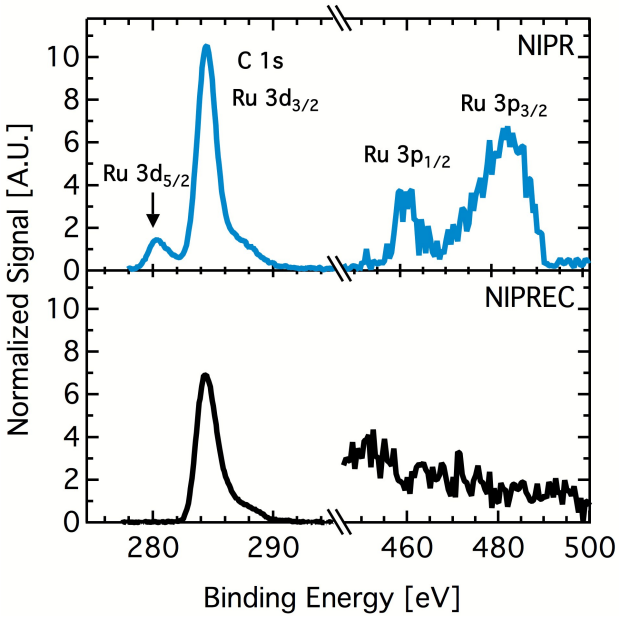

Figure 5. Ruthenium 3*d* and 3*p* XPS data for NIPR and NIPREC. The Carbon 1*s* and Ru $3d_{3/2}$ peaks overlap within the uncertainty of the binding energy.

2.4 Pt and Ru XPS

The normalized Pt 4*f* XPS data is given in Figure 4 for the NIPR and NIPREC cases. The NIPR sample condition shows a chemical shift of the Pt 4*f* doublet within the uncertainty of the measurement. This suggests that the platinum is almost entirely in metallic form. The data for the NIPREC show a shift of +1.0 ± 0.2 eV and the shape of the Pt4f doublet is not as well defined. The onset of oxidation for platinum can be measured with positive chemical shift of the binding energy.[44, 45] These results suggest the electrochemical cycling leads to some platinum oxidation.

The normalized Ru 3*d* and 3*p* XPS are shown in Figure 5. The C 1*s* and Ru $3d_{3/2}$ binding energies are very close at 384.5 eV and 384.2 eV, respectively. Some overlap is expected, but the $3d_{3/2}$ photoelectron cross section is smaller than the $3d_{5/2}$ thus the contribution to the peak near 384.5 eV is small. We included the Ru 3*p* data to support the main observation that after electrochemical cycling, the Ru signal drops below the signal detection limit. This is not surprising as Ru loss in acidic conditions is well known and a significant problem for DMFCs.

3. Experiment

3.1 Sample preparation

The experimental details of the HOPG preparation have been described in detail elsewhere.[9, 10] The samples consisted of grade 2 HOPG sized 10×10×1 mm (SPI Inc.). Ion implantation was performed at room temperature in a vacuum chamber using nitrogen gas with an ion beam energy of 100 eV, ion current of 13.5 mA and an implantation time of ~45 s with the ion beam directed 55˚ off the sample normal. The estimated ion dose for this condition was 5×10^{16} ions/cm^2. The samples were then transferred in air to a different vacuum system for metal deposition. Platinum-ruthenium was sputtered onto the HOPG surface using a 2 inch, Pt:Ru (50:50) alloy target with an Onyx magnetron II (Angstrom Science). Magnetron sputtering using argon processing gas (20 mTorr) was performed in DC mode at constant power of 20 W with ~360 V potential for 5 s.

Electrochemical cycling was performed in an aqueous solution of 1 M H_2SO_4 with the HOPG as the working electrode, a platinum counter electrode and a reference electrode of Ag/AgCl. The potential was cycled 300 times from 0 to 1.1 V vs Ag/AgCl at a scan rate of 250 mV/s. The cycling was performed using a electrochemical cell where an o-ring seal was pressed against the HOPG surface to expose an 8 mm circular area of the working electrode.

3.2 Synchrotron measurements

The NEXAFS data were collected at end station 10-1 of the Stanford Synchrotron Radiation Lightsource (SSRL) in SLAC National Accelerator Laboratory. The Beamline (10-1) uses a wiggler insertion device and a spherical grating monochromator, yielding a linear polarization of ~80%, an energy resolution ($\Delta E/E$) better than 2×10^{-4}, and a spot size of <1 mm^2. The analysis chamber is operated at a vacuum of ~10^{-9} torr and is equipped with a cylindrical mirror analyzer (CMA, PHI Inc), a Channeltron total electron yield detector, and a sample translation stage that provides *x-y-z rotation* of the sample. Auger Electron Yield was collected by measuring a wide (~2 eV) window using the CMA set at or below the main Auger energy of each element. The incoming flux was normalized by monitoring the beam flux with a gold mesh mounted upstream of the main chamber. The slits of the monochromator were opened to provide intermediate energy resolution (<0.2 eV) in the NEXAFS, and in the XPS measurements, the CMA analyzer was operated at 50 eV pass energy for a resolution of about 0.5 eV (~0.7 eV total).

The energy scale of the NEXAFS scans was calibrated by first correcting monochromator energy drifts by simultaneous collection of a reference spectra from a calibration sample intercepting a few percent of the beam upstream of the main chamber, $I_{REF}(E)$, for all scans. The reference data, $I_{REF}(E)$, were then fit to the data of the HOPG control, $I_{REF}^{HOPG}(E)$, according to:

$$I_{REF}^{HOPG}(E) = p_0 I(E+\varepsilon_0) + p_1 \quad [1]$$

with p terms being fitting constants and ε_0 providing the shift in energy of the reference relative to the HOPG control. This method enabled all data to be aligned to the same energy scale. The absolute energy scale was then determined by comparison to standards: the C 1s σ* exciton (291.65 ± 0.025 eV);[46] the nitrilic N 1s→ π* peak at 399.5 eV;[21, 22] the pre-edge peak of the O 1s for MnO_2 (529.2 eV).[47] The electron yield for the samples was normalized to the signal from a clean gold grid that was taken simultaneously with all spectra. A linear background was fitted to each data set and subtracted. The data were then area normalized over the region under the curve. XPS binding energies were calibrated to the carbon 1s peak at 284.5 eV with the uncertainty being ±0.2 eV. .

The fitting analysis was performed after removal of the NEXAFS step features, which is based on the following equation, $S(x)$, from Stöhr:[20]

$$S(x) = A * \left[\frac{1}{2} + \frac{1}{2} erf\left(2\sqrt{ln2}\frac{x-x_0}{\sigma}\right)\right], x \le x_0 + \sigma \quad [2]$$

where A is the step height, x_0 the position of the step, and σ is the step width. The processed data were fitted with Gaussian functions. The Gaussian peak area and position was fit as a free parameter whereas the peak width was either held constant or constrained so as to approximate a physical peak broadening with core-hole lifetime and vibrational broadening. In some cases for the C 1s spectra, an additional spline was subtracted to address the complex background structure.

Conclusion

We report a soft x-ray spectroscopy study of nitrogen implantation and electrochemical cycling. We find that nitrogen implantation introduces nitrogen species and defects into HOPG. The primary nitrogen species include pyridinic, nitrilic, and graphitic with no evidence of pyrolic nitrogen. Upon exposure to ambient conditions, the carbon defects react and produce both –C=O and –C-OH species. Sputtering Pt:Ru and subsequent air exposure introduces more defects that react with ambient oxygen to increase the number of –C=O species. Electrochemical cycling reduces heterogeneity in both –C-O- and –C-N- species. It also reduces unsaturated species such as –C=O and –C≡N denoted by reduction of the π* peaks for specific species such as nitrile. The result is a bonding with a stronger σ character, possibly with hydrogen termination such as –OH or –NH_2. There is no significant loss of total nitrogen area from cycling. The electrochemical cycling also leads to oxidation of the platinum and loss of ruthenium. The effects that the electrochemical processes produce on support materials used in fuel cell technologies urges more future work with these techniques. We did not observe direct evidence of a metal-support interaction most likely due to number of polydisperse carbon and nitrogen species. The results provide useful evidence of the types of nitrogen species that are present after electrochemical processes. This should be incorporated into future efforts that seek to improve the metal-support interaction within this system. Furthermore, additional theory experiments could target the effects on the metal-support interaction with the presence of amino and nitrilic side groups on a carbon surface. The acid-base chemistry of these groups should also be considered for the electrochemical reactions that are used in fuel cells.

Acknowledgements

This work was supported by the U.S. Department of Energy under Contract No. DE-AC36-08-GO28308 with the National Renewable Energy Laboratory. Portions of this research were carried out at the Stanford Synchrotron Radiation Lightsource, a Directorate of SLAC National Accelerator Laboratory and an Office of Science User Facility operated for the U.S. Department of Energy Office of Science by Stanford University.

References

1 1. S. C. Roy, A. W. Harding, A. E. Russell and K. M. Thomas, *Journal of the Electrochemical Society*, 1997, **144**, 2323-2328.
2 2. C. L. Sun, L. C. Chen, M. C. Su, L. S. Hong, O. Chyan, C. Y. Hsu, K. H. Chen, T. F. Chang and L. Chang, *Chemistry of Materials*, 2005, **17**, 3749-3753.
3 3. G. Wu, D. Li, C. Dai, D. Wang and N. Li, *Langmuir*, 2008, **24**, 3566-3575.
4 4. T. Maiyalagan, *Applied Catalysis B-Environmental*, 2008, **80**, 286-295.
5 5. Z. Lei, L. An, L. Dang, M. Zhao, J. Shi, S. Bai and Y. Cao, *Microporous and Mesoporous Materials*, 2009, **119**, 30-38.
6 6. Z. Lei, M. Zhao, L. Dang, L. An, M. Lu, A.-Y. Lo, N. Yu and S.-B. Liu, *Journal of Materials Chemistry*, 2009, **19**, 5985-5995.
7 7. M. N. Groves, A. S. W. Chan, C. Malardier-Jugroot and M. Jugroot, *Chemical Physics Letters*, 2009, **481**, 214-219.
8 8. X. Li, S. Park and B. N. Popov, *Journal of Power Sources*, 2010, **195**, 445-452.
9 9. S. Pylypenko, A. Queen, T. S. Olson, A. Dameron, K. O'Neill, K. C. Neyerlin, B. Pivovar, H. N. Dinh, D. S. Ginley, T. Gennett and R. O'Hayre, *The Journal of Physical Chemistry C*, 2011, **115**, 13667-13675.
10 10. S. Pylypenko, A. Queen, T. S. Olson, A. Dameron, K. O'Neill, K. C. Neyerlin, B. Pivovar, H. N. Dinh, D. S. Ginley, T. Gennett and R. O'Hayre, *The Journal of Physical Chemistry C*, 2011, **115**, 13676-13684.
11 11. A. R. Corpuz, T. S. Olson, P. Joghee, S. Pylypenko, A. A. Dameron, H. N. Dinh, K. J. O'Neill, K. E. Hurst, G. Bender, T. Gennett, B. S. Pivovar, R. M. Richards and R. P. O'Hayre, *Journal of Power Sources*, 2012, **217**, 142-151.
12 12. K. N. Wood, S. Christensen, S. Pylypenko, T. Olson, A. Dameron, K. Hurst, H. Dinh, T. Gennett and R. O'Hayre, *MRS Communications* 2012, **2**, 85-89.
13 13. S. Pylypenko, A. Borisevich, K. L. More, A. R. Corpuz, T. Holme, A. A. Dameron, T. S. Olson, H. N. Dinh, T. Gennett and R. O'Hayre, *Energy & Environmental Science*, 2013, **6**, 2957-2964.
14 14. T. Holme, Y. Zhou, R. Pasquarelli and R. O'Hayre, *Physical Chemistry Chemical Physics*, 2010, **12**, 9461-9468.
15 15. D. Lee, W. Lee, S. Kim and Y.-H. Kim, *Physical Review Letters*, 2011, **106**.
16 16. S. Pylypenko, A. Borisevich, K. More, A. Corpuz, T. Holme, A. Dameron, T. Olson, H. Dinh, T. Gennett and R. O'Hayre, *Energy & Environmental Science*, 2013, **accpted**.
17 17. Y. Zhou, K. Neyerlin, T. S. Olson, S. Pylypenko, J. Bult, H. N. Dinh, T. Gennett, Z. Shao and R. O'Hayre, *Energy & Environmental Science*, 2010, **3**, 1437-1446.
18 18. S. Maldonado, S. Morin and K. J. Stevenson, *Carbon*, 2006, **44**, 1429-1437.
19 19. Y. Zhou, R. Pasquarelli, T. Holme, J. Berry, D. Ginley and R. O'Hayre, *Journal of Materials Chemistry*, 2009, **19**, 7830-7838.
20 20. J. Stöhr, *NEXAFS Spectroscopy*, Springer-Verlag, New York, 2003.
21 21. I. Shimoyama, G. Wu, T. Sekiguchi and Y. Baba, *Physical Review B*, 2000, **62**, R6053-R6056.
22 22. I. Shimoyama, G. Wu, T. Sekiguchi and Y. Baba, *Journal of Electron Spectroscopy and Related Phenomena*, 2001, **114-116**, 841-848.
23 23. A. A. Dameron, T. S. Olson, S. T. Christensen, J. E. Leisch, K. E. Hurst, S. Pylypenko, J. B. Bult, D. S. Ginley, R. P. O'Hayre, H. N. Dinh and T. Gennett, *Acs Catalysis*, 2011, **1**, 1307-1315.
24 24. P. Brühwiler, A. Maxwell, C. Puglia, A. Nilsson, S. Andersson and N. Mårtensson, *Physical Review Letters*, 1995, **74**, 614-617.
25 25. D. A. Outka, J. Stohr, R. J. Madix, H. H. Rotermund, B. Hermsmeier and J. Solomon, *Surface Science*, 1987, **185**, 53-74.
26 26. S. G. Urquhart, A. P. Hitchcock, R. D. Leapman, R. D. Priester and E. G. Rightor, *J Polym Sci Pol Phys*, 1995, **33**, 1593-1602.
27 27. D. Solomon, J. Lehmann, J. Kinyangi, B. Q. Liang, K. Heymann, L. Dathe, K. Hanley, S. Wirick and C. Jacobsen, *Soil Sci Soc Am J*, 2009, **73**, 1817-1830.
28 28. J. T. Francis and A. P. Hitchcock, *J Phys Chem-Us*, 1992, **96**, 6598-6610.
29 29. R. V. Dennis, B. J. Schultz, C. Jaye, X. Wang, D. A. Fischer, A. N. Cartwright and S. Banerjee, *J Vac Sci Technol B*, 2013, **31**, 041204 (041201-041209).
30 30. M. Mauerer, P. Zebisch, M. Weinelt and H. P. Steinruck, *J Chem Phys*, 1993, **99**, 3343-3352.
31 31. D. Duflot, C. Hannay, J. P. Flament and M. J. Hubin-Franskin, *The Journal of Chemical Physics*, 1998, **109**, 5308-5318.
32 32. N. Hellgren, *Thin Solid Films*, 2005, **471**, 19-34.
33 33. I. Jimenez, W. M. Tong, D. K. Shuh, B. C. Holloway, M. A. Kelly, P. Pianetta, L. J. Terminello and F. J. Himpsel, *Appl Phys Lett*, 1999, **74**, 2620-2622.
34 34. J. A. Horsley, J. Stöhr, A. P. Hitchcock, D. C. Newbury, A. L. Johnson and F. Sette, *J Chem Phys*, 1985, **83**, 6099-6107.
35 35. S. Pylypenko, A. Queen, T. S. Olson, A. Dameron, K. O'Neill, K. C. Neyerlin, B. Pivovar, H. N. Dinh, D. S. Ginley, T. Gennett and R. O'Hayre, *Journal of Physical Chemistry C*, 2011, **115**, 13667-13675.
36 36. R. Gago, I. Jiménez, J. Neidhardt, B. Abendroth, I. Caretti, L. Hultman and W. Möller, *Physical Review B*, 2005, **71**, 125414 (125411-125416).
37 37. H. Niwa, K. Horiba, Y. Harada, M. Oshima, T. Ikeda, K. Terakura, J.-i. Ozaki and S. Miyata, *Journal of Power Sources*, 2009, **187**, 93-97.
38 38. J. M. Ripalda, E. Román, L. Galán, I. Montero, S. Lizzit, A. Baraldi, G. Comelli, G. Paolucci and A. Goldoni, *The Journal of Chemical Physics*, 2003, **118**, 3748-3755.
39 39. T. Schiros, D. Nordlund, L. Palova, D. Prezzi, L. Y. Zhao, K. S. Kim, U. Wurstbauer, C. Gutierrez, D. Delongchamp, C. Jaye, D. Fischer, H. Ogasawara, L. G. M. Pettersson, D. R. Reichman, P. Kim, M. S. Hybertsen and A. N. Pasupathy, *Nano Lett*, 2012, **12**, 4025-4031.
40 40. S. Narioka, H. Ishii, Y. Ouchi, T. Yokoyama, T. Ohta and K. Seki, *J Phys Chem-Us*, 1995, **99**, 1332-1337.
41 41. G. Polzonetti, V. Carravetta, G. Iucci, A. Ferri, G. Paolucci, A. Goldoni, P. Parent, C. Laffon and M. V. Russo, *Chem Phys*, 2004, **296**, 87-100.
42 42. A. P. Hitchcock, Gas Phase Core Excitation Database, http://unicorn.mcmaster.ca/corex/cedb-title.html).
43 43. A. P. Hitchcock and D. C. Mancini, *Journal of Electron Spectroscopy and Related Phenomena*, 1994, **67**, 1-132.
44 44. M. Peuckert, F. P. Coenen and H. P. Bonzel, *Electrochimica Acta*, 1984, **29**, 1305-1314.
45 45. *NIST X-ray Photoelectron Spectroscopy Database, v. 4.1* National Institute of Standards and Technology, Gaithersburg, Maryland: 2012.

46 46. B. Watts and H. Ade, *Journal of Electron Spectroscopy and Related Phenomena*, 2008, **162**, 49-55.
47 47. B. Gilbert, B. H. Frazer, A. Belz, P. G. Conrad, K. H. Nealson, D. Haskel, J. C. Lang, G. Srajer and G. De Stasio, *Journal of Physical Chemistry A*, 2003, **107**, 2839-2847.

Tables

Table 1. C 1*s* π* fitting results

Peak➔ / Conditions➘	1	2	3	4	5
NI	285.5		288*	288.5	291.6
NIPR	285.3	286.1	287.8	288.5	
NIPREC	285.4			288.6	

*Determined graphically.

Table 2. N 1*s* fitting results

Peak➔ / Conditions➘	1	2	3	4	5	Total Area [A.U.]
NI	398.6	399.6	400.9	404.7	409.5	7.8
NIPR	398.5	399.6	400.8	404.4	410.8	9.40
NIPREC	398.4	399.6	400.8	405.5	408.9	10.0

Table 3. O 1*s* fitting results

Peak➔ / Conditions➘	1	2	3	4	5	Total Area [A.U.]
NI	531.3	536.3		542.1		1.95
NIPR	531.8		538.4	543.8	562.5	11.4
NIPREC	531.5	536.7	537.5	542.5	561.0	14.4

Table of Contents Figure

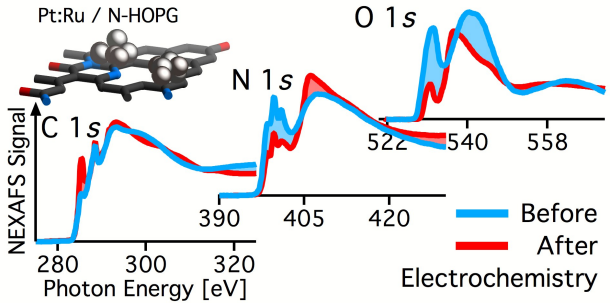

X-ray absorption spectroscopy shows the dramatic changes a nitrogen modified carbon support can undergo due to electrochemical processes.